Results in Applied Mathematics 25 (2025) 100528

Contents lists available at ScienceDirect

Results in Applied Mathematics

journal homepage: www.elsevier.com/locate/results-in-applied-mathematics

(2 + 1)-dimensional discrete exterior discretization of a general wave model in Minkowski spacetime

Sanna Mönkölä *, Jukka Räbinä, Tytti Saksa, Tuomo Rossi

Faculty of Information Technology, University of Jyvaskyla, Jyvaskyla, Finland

ARTICLE INFO

Keywords:
Discrete exterior calculus
Minkowski spacetime
General model
Wave equations

ABSTRACT

We present a differential geometry-based model for linear wave equations in (2+1)-dimensional spacetime. This model encompasses acoustic, elastic, and electromagnetic waves and is also applicable in quantum mechanical simulations. For discretization, we introduce a spacetime extension of discrete exterior calculus, resulting in a leapfrog-style time evolution. The scheme further supports numerical simulations of moving and deforming domains. The numerical tests presented in this paper demonstrate the method's stability limits and computational efficiency.

1. Introduction

Understanding the propagation of waves in spacetime presents a fundamental challenge with implications across various scientific domains, including acoustics, elasticity, electromagnetism, and quantum mechanics. A primary difficulty in deriving a general model arises from attempts at unification, which often focus on combining incompatible, problem-specific models. A potential remedy is to return to the basics and seek the most general paradigm, shifting the focus from physical phenomena and observations to a theoretical viewpoint. The authors have identified two promising concepts for unifying and generalizing classical vector analysis: the exterior calculus of differential forms on manifolds [1] and Clifford geometric algebra with multivectors defined in pseudo-Euclidean spacetime [2].

Several publications have introduced the Maxwell equations with differential forms (see, e.g., [3–6]), but neither of the concepts has been generalized to a wider class of boundary value problems. We construct a real-valued spacetime algebra as a Clifford algebra with the Minkowski metric, presenting all physical quantities in spacetime as multivectors [7]. At each point of a flat spacetime manifold, the spacetime algebra is reproduced as a tangent algebra, with locally defined multivectors [8]. The spacetime points and their tangent algebras form a Clifford bundle, which serves as the framework for defining multivector fields, such as electromagnetic, acoustic, elastic, or quantum mechanical fields. The geometric construction facilitates a natural unification of various wave models (see also [9,10]).

Over the past few decades, several computational tools based on problem-specific methods have been constructed, particularly in the context of finite element methods. However, these often encounter challenges when addressing complex geometries, discontinuities in solutions, and the preservation of geometric properties. In the discontinuous Galerkin method, there are no global continuity requirements, but each spacetime element only couples with the neighboring element by the face terms.

Cartan [11] introduced exterior calculus as a coordinate-free approach for handling differential forms on manifolds. Building on this foundational work, discrete exterior calculus (DEC) [12,13] discretizes differential geometric quantities in a way that inherently preserves the structure of the underlying smooth theory. It also relates to Tonti's classification of physical variables and laws into primal and dual formulations [14,15].

* Corresponding author.
E-mail address: sanna.monkola@jyu.fi (S. Mönkölä).

https://doi.org/10.1016/j.rinam.2024.100528
Received 22 January 2024; Received in revised form 1 November 2024; Accepted 5 December 2024
Available online 16 December 2024

The early stages of the DEC, as a generalization of the finite difference time domain (FDTD) method [16], were introduced in electromagnetics by Bossavit and Kettunen [17]. Hirani [18] presented a rigorous computational tool that provides a framework for discretizing differential forms, exterior derivatives, and the Hodge star operator, which led to the development of PyDEC software [19]. Räbinä [20,21] implemented a general-purpose C++ library employing DEC formalism. More recently, Myyrä published a discrete exterior calculus toolkit for Rust [22], which is currently under active development.

DEC discretization has been applied in several studies to static or time-harmonic problems from which time derivatives are absent. Application areas include elastics [23], electromagnetics [24,25], quantum mechanics [26], and fluid problems [27]. In dynamic problems, the system of partial differential equations is traditionally transformed into a system of ordinary differential equations in time, which can then be solved using numerical integration. This classical approach, with DEC discretization in space, has found applications across various fields, including computer graphics [28,29], acoustics [30], electromagnetics [31–34], quantum mechanics [35–37], and fluid dynamics [38]. For electromagnetics discretized with DEC, the mathematical aspects of convergence and stability are discussed in [33,39], while for Poisson problems, stability, consistency, and convergence are proved in [40]. Error bounds for discrete Hodge operators are considered in [41] in a general context. Toshniwal and Hughes introduced isogeometric discrete differential forms [42], while Lohi et al. enhanced the method using higher-order Whitney forms [43–46]. An essential feature that differentiates spacetime methods from the more classical approaches to dynamic boundary value problems is the separation in space and time in discretization.

The early inspiration for discrete geometric approaches in spacetime, based on the Voronoi and Delaunay lattices, was a mathematical formalism called Regge Calculus (RC), a discretized form of Einstein's general relativity developed by Regge [47]. RC has been applied in both classical and quantum general relativity (see [48], and references therein). Later, Sorkin presented the mathematical principles of causal sets to discretize spacetime [49]. Our preliminary results on spacetime simulations using discrete exterior discretizations are presented in [50,51]. Our method relies on Voronoi–Delaunay tessellation and enables simulations in domains that undergo motions and deformations. Such simulations are known to be challenging using finite element approaches, but some progress has also been made in that field, such as with unfitted finite elements (see, e.g., [52,53], and references therein).

The rest of this article is organized as follows. In Section 2, we generalize the linear (2+1)-dimensional wave model by employing a Clifford algebra in Minkowski spacetime. We first introduce a multivector representation and then transition to differential form formulation. Section 3 presents the spacetime discretization using discrete exterior calculus, which is a natural choice for the differential form formulation. One of the key contributions of our work lies in the computational software and numerical tests conducted to show the performance of the method. In Section 4, we demonstrate the accuracy and stability conditions of five different types of computational meshes. We also simulate a nonconvex spatial obstacle rotating around the time axis.

2. Spacetime model

We present a general model for linear wave equations in $(2+1)$ dimensions based on a Clifford algebra in Minkowski spacetime $\mathbb{R}^{1,2}$. That is, we have a Euclidean space $(x_1, x_2)^T$, imaginary time $x_0 = \mathrm{i}ct$, and orthonormal basis vectors γ_i, $i = 0, 1, 2$, such that $\gamma_0\gamma_0 = -1$ and $\gamma_i\gamma_i = 1$ for $i = 1, 2$. The unit pseudoscalar is $\mathrm{i} = \gamma_0\gamma_1\gamma_2$. The geometric product of two vectors, a and b, can be presented by $ab = a \cdot b + a \wedge b$, where $a \cdot b$ is the dot product and $a \wedge b = \mathrm{i}a \times b$ is the exterior product (wedge product). The geometric product of the basis vectors is associative and distributive, and $\gamma_i\gamma_j = -\gamma_j\gamma_i$ for $i \neq j$.

2.1. Multivector presentation

The basis for $(2 + 1)$-dimensional geometric algebra is set by 2^3 blades that are 1, γ_0, γ_1, γ_2, $(\gamma_0 \wedge \gamma_1)$, $(\gamma_0 \wedge \gamma_2)$, $(\gamma_1 \wedge \gamma_2)$, and $(\gamma_0 \wedge \gamma_1 \wedge \gamma_2)$. In general, the basis k-blades are wedge products of k basis vectors that span a k-dimensional subspace. The wedge product of two vectors results in a two-dimensional subspace called bivector (2-vector), and the wedge product of three vectors results in a three-dimensional trivector (3-vector) space. In a three-dimensional space, a general element, presented as a linear combination of the basis blades, with coefficients f_i, $i = 1, \ldots, 8$, is

$$F = f_1 + f_2\gamma_0 + f_3\gamma_1 + f_4\gamma_2 + f_5(\gamma_0 \wedge \gamma_1) + f_6(\gamma_0 \wedge \gamma_2) + f_7(\gamma_1 \wedge \gamma_2) + f_8(\gamma_0 \wedge \gamma_1 \wedge \gamma_2). \tag{1}$$

Respectively, we present, with coefficients b_i, $i = 1, \ldots, 8$, a general source term,

$$J = b_1 + b_2\gamma_0 + b_3\gamma_1 + b_4\gamma_2 + b_5(\gamma_0 \wedge \gamma_1) + b_6(\gamma_0 \wedge \gamma_2) + b_7(\gamma_1 \wedge \gamma_2) + b_8(\gamma_0 \wedge \gamma_1 \wedge \gamma_2). \tag{2}$$

By operating F by the spacetime gradient $\boldsymbol{\nabla} = -\gamma_0\partial_0 + \gamma_1\partial_1 + \gamma_2\partial_2$, we get

$$\left(\begin{array}{c|ccc|ccc|c}
 & \partial_0 & \partial_1 & \partial_2 & & & & \\
\hline
-\partial_0 & & & & -\partial_1 & -\partial_2 & & \\
\partial_1 & & & & \partial_0 & & -\partial_2 & \\
\partial_2 & & & & & \partial_0 & \partial_1 & \\
\hline
 & -\partial_1 & -\partial_0 & & & & & \partial_2 \\
 & -\partial_2 & & -\partial_0 & & & & -\partial_1 \\
\hline
 & & -\partial_2 & \partial_1 & & & & \partial_0 \\
\hline
 & & & & \partial_2 & -\partial_1 & -\partial_0 &
\end{array}\right)
\left(\begin{array}{c} f_1 \\ \hline f_2 \\ f_3 \\ f_4 \\ \hline f_5 \\ f_6 \\ \hline f_7 \\ \hline f_8 \end{array}\right)
=
\left(\begin{array}{c} b_1 \\ \hline b_2 \\ b_3 \\ b_4 \\ \hline b_5 \\ b_6 \\ \hline b_7 \\ \hline b_8 \end{array}\right). \tag{3}$$

Remark 2.1. Acoustic wave equation: By setting, in Eq. (3), $f_1 = f_5 = f_6 = f_7 = f_8 = 0$, f_3 and f_4 can be associated with horizontal and vertical velocity components and f_2 with pressure.

Remark 2.2. Electromagnetic wave equation: By setting, in Eq. (3), $f_1 = f_2 = f_3 = f_4 = f_8 = 0$ and associating f_7 with the third component of the magnetic field strength and f_5 and f_6 with the first and second components of the electric field strength, we obtain the transverse electric mode of the Maxwell equation. Respectively, by setting $f_1 = f_5 = f_6 = f_7 = f_8 = 0$ and associating f_2 with the third component of the electric field strength and f_3 and f_4 with the second and first components of the magnetic field strength, we get the transverse magnetic mode of the Maxwell equation.

2.2. Differential form formulation

Based on the dual correspondence between k-vectors and k-differential forms [54], we turn to a differential form representation, where the differentials dx_0, dx_1, and dx_2 are basis 1-forms and basis 2-forms are constructed as wedge (exterior) products of two basis 1-forms, such that $dx_i \wedge dx_i = 0$ and $dx_i \wedge dx_j = -dx_j \wedge dx_i$. Respectively, $dx_0 \wedge dx_1 \wedge dx_2$ is a basis 3-form.

With differential multiforms

$$\tilde{F} = \tilde{f}_1 + \tilde{f}_2 dx_0 + \tilde{f}_3 dx_1 + \tilde{f}_4 dx_2 + \tilde{f}_5 (dx_0 \wedge dx_1) + \tilde{f}_6 (dx_0 \wedge dx_2) + \tilde{f}_7 (dx_1 \wedge dx_2) + \tilde{f}_8 (dx_0 \wedge dx_1 \wedge dx_2) \tag{4}$$

and

$$\tilde{J} = \tilde{b}_1 + \tilde{b}_2 dx_0 + \tilde{b}_3 dx_1 + \tilde{b}_4 dx_2 + \tilde{b}_5 (dx_0 \wedge dx_1) + \tilde{b}_6 (dx_0 \wedge dx_2) + \tilde{b}_7 (dx_1 \wedge dx_2) + \tilde{b}_8 (dx_0 \wedge dx_1 \wedge dx_2), \tag{5}$$

we can present $(2+1)$-dimensional linear wave models in a three-dimensional pseudo-Riemannian manifold as

$$\partial \tilde{F} = \tilde{J}, \tag{6}$$

or

$$\partial \star \tilde{F} = \star \tilde{J}, \tag{7}$$

where $\partial = (\boldsymbol{d} + \boldsymbol{\delta})$ is the differential operator that is the sum of the exterior derivative $\boldsymbol{d}$ and its coderivative (interior derivative) $\boldsymbol{\delta} = (-1)^k \star^{-1} \boldsymbol{d} \star$ and $\star$ is the Hodge star operator. In particular,

$$\begin{aligned} \boldsymbol{d}\tilde{F} =& -\partial_0 \tilde{f}_1 dx_0 + \partial_1 \tilde{f}_1 dx_1 + \partial_2 \tilde{f}_1 dx_2 - (\partial_0 \tilde{f}_3 + \partial_1 \tilde{f}_2)(dx_0 \wedge dx_1) - (\partial_0 \tilde{f}_4 + \partial_2 \tilde{f}_2)(dx_0 \wedge dx_2) + (\partial_1 \tilde{f}_4 - \partial_2 \tilde{f}_3)(dx_1 \wedge dx_2) \\ &+ (\partial_2 \tilde{f}_5 - \partial_1 \tilde{f}_6 - \partial_0 \tilde{f}_7)(dx_0 \wedge dx_1 \wedge dx_2), \end{aligned} \tag{8}$$

$$\begin{aligned} \boldsymbol{\delta}\tilde{F} =& \partial_0 \tilde{f}_2 + \partial_1 \tilde{f}_3 + \partial_2 \tilde{f}_4 - (\partial_1 \tilde{f}_5 + \partial_2 \tilde{f}_6) dx_0 + (\partial_0 \tilde{f}_5 - \partial_2 \tilde{f}_7) dx_1 + (\partial_0 \tilde{f}_6 + \partial_1 \tilde{f}_7) dx_2 \\ &+ \partial_2 \tilde{f}_8 (dx_0 \wedge dx_1) - \partial_1 \tilde{f}_8 (dx_0 \wedge dx_2) + \partial_0 \tilde{f}_8 (dx_1 \wedge dx_2). \end{aligned} \tag{9}$$

Eqs. (6) and (7) are dual to each other. For instance, electromagnetic problems with electric field strength and magnetic flux density are presented by Eq. (6) and with electric flux density and magnetic field strength by Eq. (7).

3. Discretization

We perform the spacetime discretization using the DEC. In principle, the procedure is similar than applied to space discretization (see, e.g., [21,28,31,55]). First, we provide the computational domain with two meshes: a primal mesh and a dual mesh. The dual mesh, formed as the Delaunay dual of the primal mesh, is orthogonal to the primal mesh under the Minkowski inner product. Each mesh is a cell complex with such a hierarchy that a 0-cell is a vertex, a 1-cell is an edge between two 0-cells, a 2-cell is a face surrounded by edges, and a 3-cell is a volume element surrounded by faces. Each primal k-cell is associated with a corresponding dual $(n-k)$-cell.

In general, in a discretized n-dimensional manifold, or a cell complex, a k-form is an object that can be integrated over k-dimensional, $0 \le k \le n$, submanifolds, or elements of the mesh. Discrete differential forms as cochains formalize the assignment of values to these k-dimensional cells. That is, the variables can be associated with nodes (0-forms), edges (1-forms), faces (2-forms), or volumes (3-forms). A discrete k-form corresponding to a differential form α_k is

$$u_k = \int_{C_k} \alpha_k = \begin{pmatrix} \int_{C_{k1}} \alpha_k \\ \vdots \\ \int_{C_{kn_k}} \alpha_k \end{pmatrix}, \tag{10}$$

where C_{ki} is the ith k-cell and n_k is the number of k-cells in the mesh.

At the discrete level, the exterior derivative is presented as an incidence matrix d_k that operates discrete differential k-forms u_k and represents the neighboring relations and relative orientations. It describes the relationships between the k-dimensional cells and their $(k-1)$-dimensional boundaries such that the entries of the matrix indicate whether a particular k-cell is incident to a particular $(k-1)$-cell. Since the Stokes theorem holds exactly, $d_k u_k = d_k \int_{C_k} \alpha_k = \int_{C_{k+1}} d\alpha_k$, the discrete differential operator d_k is exact.

The discrete counterpart to the Hodge operator is matrix $\star_k$ mapping between the primal and dual mesh. It is diagonal by construction if the dual elements are orthogonal to the primal elements. Essentially, it is a map from discrete differential k-forms on a mesh to a discrete differential $(n-k)$-form on the dual mesh and includes metric and material properties.

The discretized general model for linear wave equations in four dimensions without external forces is

$$\left(\begin{array}{cc|cc|cc} & \delta_{0s} & \frac{1}{\Delta t^2}d_{0t} & & & \\ \hline d_{0s} & & & \delta_{1s} & \frac{1}{\Delta t^2}d_{1t} & \\ d_{0t} & & & & -\delta_{0s} & \\ \hline & d_{1s} & & & & \frac{1}{\Delta t^2}d_{2t} \\ & d_{1t} & -d_{0s} & & & -\delta_{1s} \\ \hline & & & d_{2t} & -d_{1s} & \end{array}\right)\left(\begin{array}{c} u_{0s} \\ \hline u_{1s} \\ u_{1t} \\ \hline u_{2s} \\ u_{2t} \\ \hline u_{3t} \end{array}\right) = 0, \tag{11}$$

where discrete k-forms u_k and incidence matrices d_k and the corresponding co-operators δ_k are constructed by spatial (subscript s) and temporal (subscript t) components. As a consequence of the model (11), we get a leapfrog-style time-stepping.

4. Numerical examples

The simulations presented in this section are performed using in-house software implemented in C++ and based on the DEC software library discussed in, for example, [21,50]. The results are carried out on a laptop with an Intel Core i5-5300U processor at 2.30 GHz.

4.1. Accuracy and stability

We solve, over the time interval $[0,T]$ within the spatial domain $\Omega = [0,1]\times[0,1]$, an transverse electric electromagnetic problem with

$$\tilde{F} = B_3(dx_1\wedge dx_2) + E_1(dx_0\wedge dx_1) + E_2(dx_0\wedge dx_2) = \tilde{B}^{\mathrm{s}} - \tilde{E}^{\mathrm{s}}\wedge dx_0, \tag{12}$$

$$\tilde{J} = J_2(dx_0\wedge dx_1) - J_1(dx_0\wedge dx_2) = \tilde{J}^{\mathrm{s}}\wedge dx_0, \tag{13}$$

$$J_1 = -\left(2x_0(x_1^2-x_1^3)(x_2-x_2^2) + \frac{1}{3}x_0^3x_2(-5x_2+12x_1x_2-10x_1+4)\right), \tag{14}$$

$$J_2 = -\left(2x_0(x_1-x_1^2)(x_2^2-x_2^3) - \frac{1}{3}x_0^3x_1(-5x_1+12x_1x_2-10x_2+4)\right), \tag{15}$$

where x_0 is time, $\mathbf{x} = (x_1,x_2)$ contains spatial variables, $\tilde{B}^{\mathrm{s}} = B_3dx_1\wedge dx_2$ is a two-form, and $\tilde{E}^{\mathrm{s}} = E_1dx_1 + E_2dx_2$ and $\tilde{J}^{\mathrm{s}} = J_1dx_2 - J_2dx_1$ are one-forms. Here, E_1 and E_2 are the spatially horizontal and vertical components of the electric field, and B_3 is the magnetic flux perpendicular to the electric field. The model assumes that there are no horizontal or vertical components of the magnetic field or the electric field component perpendicular to them.

The formulation above also satisfies

$$d_s\tilde{H}^{\mathrm{s}} = \frac{\partial\tilde{D}^{\mathrm{s}}}{\partial x_0} - \tilde{J}^{\mathrm{s}}, \tag{16}$$

$$d_s\tilde{E}^{\mathrm{s}} = -\frac{\partial\tilde{B}^{\mathrm{s}}}{\partial x_0}, \tag{17}$$

where time and space are separated from each other, d_s is the spatial exterior derivative, $\frac{\partial}{\partial x_0}$ is the time derivative, $\tilde{D}^{\mathrm{s}} = D_1dx_2 - D_2dx_1$ is a one-form, and $\tilde{H}^{\mathrm{s}} = H_3$ is a zero-form. With (16)–(17), the constitutive relations are $\tilde{D}^{\mathrm{s}} = \star_\varepsilon\tilde{E}^{\mathrm{s}}$ and $\tilde{B}^{\mathrm{s}} = \star_\mu\tilde{H}^{\mathrm{s}}$, where $\star_\varepsilon$ and $\star_\mu$ are the Hodge operators, related to permittivity ε and permeability μ, mapping a differential k-form to a differential $n-k$ form in an n-dimensional space. Respectively, in three-dimensional spacetime, the spatial one- and two-forms $\tilde{E}^{\mathrm{s}}$ and $\tilde{B}^{\mathrm{s}}$ have as their dual counterparts spacetime two-form $\tilde{D} = D_1(dx_2\wedge dx_0) - D_2(dx_1\wedge dx_0)$ and temporal one-form $\tilde{H} = H_3\wedge dx_0$.

Given the spacetime context, we interpret both the initial conditions,

$$E_1(\mathbf{x},0) = E_2(\mathbf{x},0) = H_3(\mathbf{x},0) = 0, \qquad \text{in } \Omega, \tag{18}$$

$$\frac{\partial E_1(\mathbf{x},0)}{\partial x_0} = \frac{\partial E_2(\mathbf{x},0)}{\partial x_0} = \frac{\partial H_3(\mathbf{x},0)}{\partial x_0} = 0, \qquad \text{in } \Omega, \tag{19}$$

and boundary conditions,

$$n_3E_2(\mathbf{x},x_0) = 0, n_3E_1(\mathbf{x},x_0) = 0, n_1E_2(\mathbf{x},x_0) = n_2E_1(\mathbf{x},x_0), \qquad \text{on } \partial\Omega\times[0,T], \tag{20}$$

$$n_2H_3(\mathbf{x},x_0) = \frac{1}{3}n_2x_0^3x_1x_2(-5x_1+6x_1x_2-5x_2+4), \qquad \text{on } \partial\Omega\times[0,T], \tag{21}$$

$$n_1H_3(\mathbf{x},x_0) = -\frac{1}{3}n_1x_0^3x_1x_2(-5x_1+6x_1x_2-5x_2+4), \qquad \text{on } \partial\Omega\times[0,T], \tag{22}$$

where n_i, $i=1,2,3$ are the components of the outward pointing unit normal, as conditions imposed along the spacetime boundary. The electric permittivity and magnetic permeability are chosen to be equal to one.

The computational domain is discretized by a mesh of vertices, edges, surfaces, and volumes. In full (2+1)-dimensional spacetime, the orthogonality of the dual mesh is defined by the Minkowski metric, which differs from the Euclidean treatment in the time

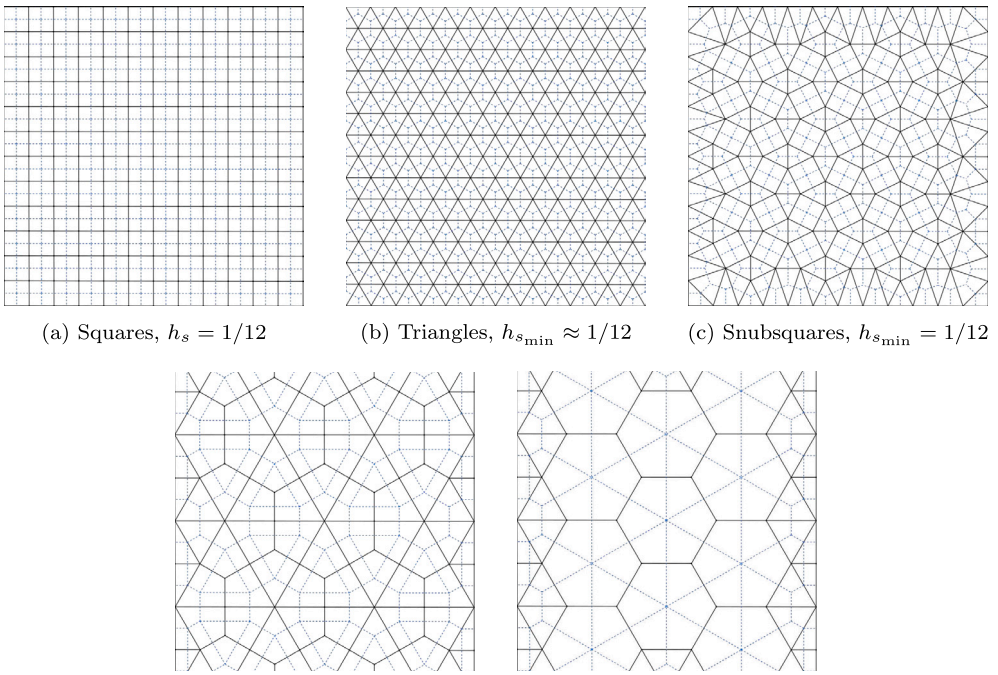

(a) Squares, $h_s = 1/12$ (b) Triangles, $h_{s_{\min}} \approx 1/12$ (c) Snubsquares, $h_{s_{\min}} = 1/12$

(d) Tetrilles, $h_{s_{\min}} = 1/12$ (e) Hexagons, $h_{s_{\min}} = 1/12$

Fig. 1. Primal (black solid line) and dual (blue dashed line) spatial tesselations.

dimension. In principle, within the spatial domain Ω, we have 2D primal mesh structures constructed of squares, triangles, snubsquares, tetrilles, or hexagons. The primal meshes and their dual counterparts are presented as cross-sections, restricted to the spatial (x_1, x_2) plane at time $x_0 = 0$, in Fig. 1. We define the discrete differential 1-forms E on primal edges and H on dual edges. Respectively, we can define the discrete differential 2-forms $\mathsf{B} = \star_2^{-1}\mathsf{H}$ on primal faces and $\mathsf{D} = \star_1\mathsf{E}$ on dual faces.

The spatial mesh step size is denoted as h_s. For meshes with elements of varying sizes, we denote the shortest spatial edge length of the primal mesh as $h_{s_{\min}}$. For the time direction, we use uniform mesh step size h_t. The spatial 2D structure repeats itself in the time direction, which is why we do not need to store the whole (2+1)D mesh structure. The temporal refinement does not increase the memory requirement since the whole (2+1)D mesh is not stored. The spacetime-stepping is staggered both in space and time, and, in principle, we could proceed in any of the spatial or temporal directions.

To consider the accuracy and stability of the method, we compare the numerical solution with the exact solution. The error is measured at $x_0 = 1$ as a discrete ℓ^2- norm $\|\mathsf{E} - \mathsf{E}_{\text{exact}}\|_2 = \sqrt{(\mathsf{E} - \mathsf{E}_{\text{exact}})^{\mathsf{T}}(\mathsf{E} - \mathsf{E}_{\text{exact}})}$, where E is the numerical solution vector (discrete 1-form) and $\mathsf{E}_{\text{exact}}$ is the line-integrated exact electric field strength vector with components $\mathsf{E}_{\text{exact}_j} = \int_{\mathcal{E}_j} \mathbf{E} \cdot dl$, where $\mathbf{E}$ is the analytical solution of the electric field given by the vector

$$\mathbf{E}(x_1, x_2, x_0) = \begin{pmatrix} x_0^2 x_2 (x_1 - x_1^2)(x_2 - x_2^2) \\ -x_0^2 x_1 (x_1 - x_1^2)(x_2 - x_2^2) \\ 0 \end{pmatrix}. \tag{23}$$

Respectively, the analytical solution of the magnetic field strength $\mathbf{H}$ is

$$\mathbf{H}(x_1, x_2, x_0) = \begin{pmatrix} 0 \\ 0 \\ \frac{1}{3} x_0^3 x_1 x_2 (-5x_1 + 6x_1 x_2 - 5x_2 + 4) \end{pmatrix}. \tag{24}$$

While proceeding in the time direction with a spatial mesh constructed of squares, the update formulas are the same as in the conventional FDTD method with separated space and time discretization. Accordingly, for the stability of the numerical scheme, the Courant–Friedrichs–Lewy (CFL) condition based on the eigenvalue criterion presented in [56] holds. That is, the scheme with a square mesh is stable, with $h_t \leq h_s/\sqrt{2}$ (see Fig. 2(a)). For a triangle mesh, the stability condition is $h_t \leq h_{s_{\min}}/\sqrt{6}$ (see Fig. 2(b)). Numerical tests also reveal the stability limits of the form $h_t \leq h_{s_{\min}}/\beta$ for other mesh types. For the snubsquare mesh, $\beta \approx 2.613$; the tetrille mesh $\beta \approx 1.401$; and the hexagon mesh $\beta \approx 1.394$ (see Figs. 2(c)–2(e)).

The accuracy of the solution can be improved by refining the temporal discretization with only the square mesh. In other cases, the level of accuracy of spatial discretization is already achieved with the largest stable temporal mesh stepsize. In these tests, the uniformity of the primal mesh correlates with a more accurate result within a fixed CPU time (see Fig. 3). That is, in a unit square

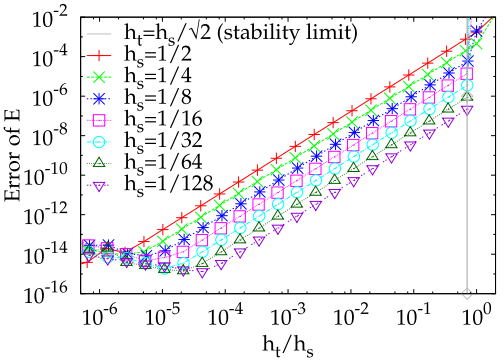

(a) Square mesh for spatial discretization.

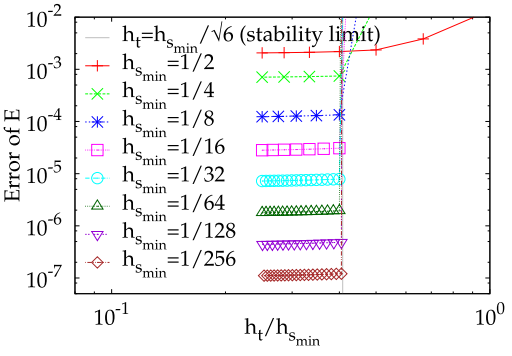

(b) Triangle mesh for spatial discretization.

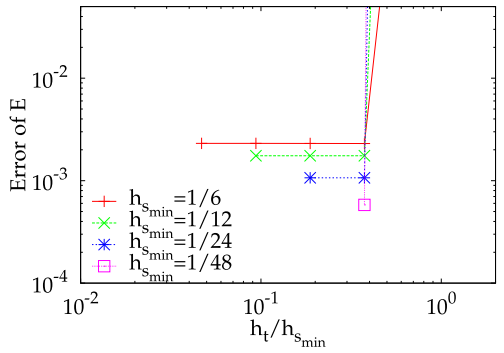

(c) Snubsquare mesh for spatial discretization

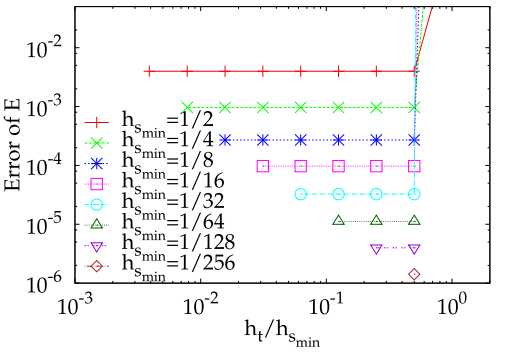

(d) Tetrille mesh for spatial discretization

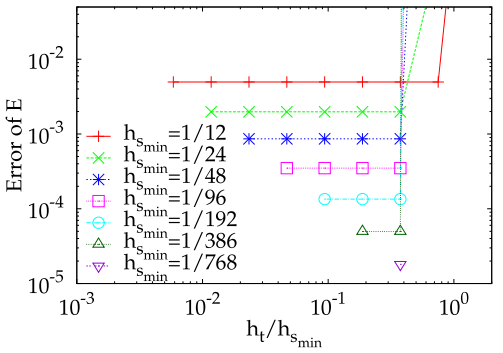

(e) Hexagon mesh for spatial discretization

Fig. 2. Error of the line-integrated electric field strength with respect to h_t/h_s for different mesh types.

spatial domain, simulations with a square mesh are computationally the most efficient. This is because other meshes have relatively smaller edge lengths near the domain boundaries, requiring finer temporal discretization to satisfy the CFL condition compared to other parts of the domain. Nevertheless, when utilizing more complex computational domains, the computational efficiency can be improved using mesh types other than the square grid.

4.2. Rotating obstacle

In this section, we consider a spacetime mesh wrapped around the time axis and show the method's capability to handle rotating domains. The cross-sectional profile of a boomerang-shaped spatial cavity rotates clockwise at a constant speed, covering an angle

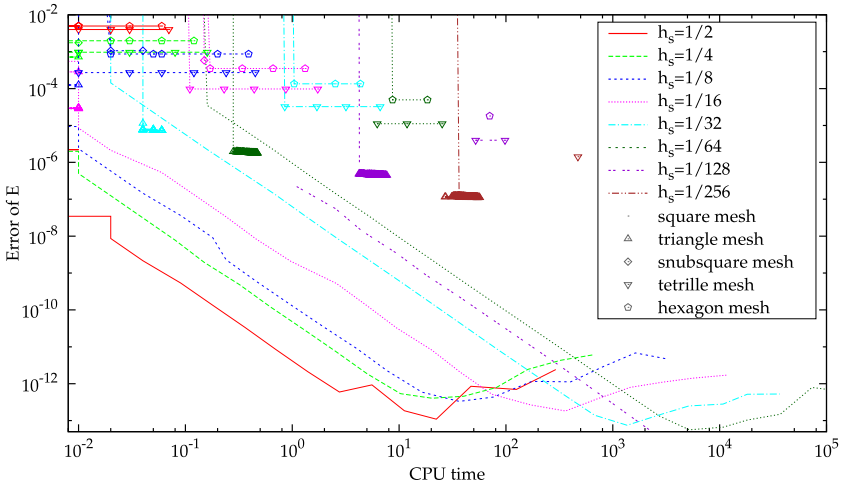

Fig. 3. Error of the line-integrated electric field strength with respect to CPU time in seconds for square, triangle, snubsquare, tetrille, and hexagon meshes with spatial and temporal refinements.

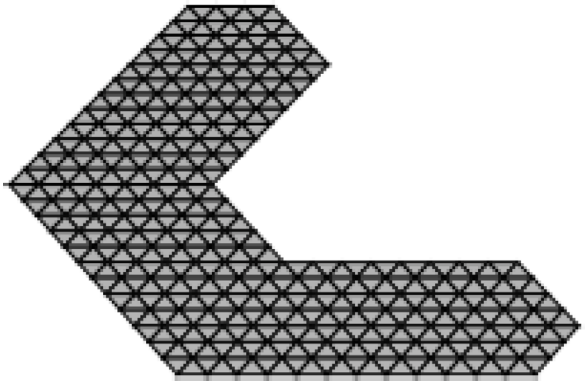

Fig. 4. Boomerang-shaped obstacle with $h_s = 1/12$.

of θ within a time interval of 0.1. In this case, the spatial domain is tessellated with triangles, and the spatial edge length h_s remains constant throughout the entire spatial domain within the triangular mesh (see Fig. 4). The selected shape of the spatial domain, along with this mesh construction, eliminates errors arising from geometry approximation in the primal mesh. Hence, it is a preferable option for this test compared to the square mesh. Furthermore, in Section 4.1, the triangle mesh yielded more accurate results within a fixed CPU time than the snubsquare, tetrahedral, or hexagon meshes.

The spacetime discretization is accomplished by introducing in the time direction discretization, which can be performed either synchronously or asynchronously (see Fig. 5). In synchronous time-stepping, we use constant time instants to compute the values in the spatial plane, i.e. all vertices of the faces of the spatial mesh are at the same time level. In asynchronous time-stepping, the time instant depends on the node positions of the spatial mesh analogous to pitching tents over a planar triangulation (see, e.g., [57,58]). The advantage of asynchronous time-stepping is that there are temporal mesh stepsizes relatively smaller than the spatial mesh stepsizes compared to synchronous time-stepping. Thus, when the number of mesh edges is fixed, the stability condition for asynchronous time-stepping is less strict than the stability condition for synchronous time-stepping. When variables are evaluated at different times, values can be interpolated to a fixed time point, though interpolation error may affect the accuracy of the solution.

First, we demonstrate the spatial cavity with edge length $h_s = 1/40$ rotating clockwise with an angle of $\theta = \pi/12$ with synchronous time-stepping and a timestep length of $h_t = 1/100$. The primal mesh has 29952 nodes, 194068 edges, 320834 faces, and 156717 volumes. The problem we solve is (12)–(13), where $\tilde{J} = 0$ and the wave source is set at the beginning of the simulation by discrete 2-form values, corresponding to $B_3 = 3(1 + \cos(50l))$, on the mesh faces whose center of mass is closer than the distance $l = \pi/50$ to the point located 12 edge lengths horizontally from the tip of the trailing boomerang arm. In the chosen coordinates, this point is at (−0.3, 0.6). All other initial and source values are set to zero. The boundaries of the cavity are assumed to be rigid, forming a perfect electric conductor that confines the electromagnetic wave within the domain and causes total reflection on the boundary. The simulation of this rotating cavity resonator is carried out with a wave speed of 1.0 until time $x_0 = 7.2$ is reached. The snapshots of the total wave pattern, as the wave is scattered by the moving cavity boundaries, are presented in Fig. 6 at $x_0 = x_{0_i} = 9i/5$,

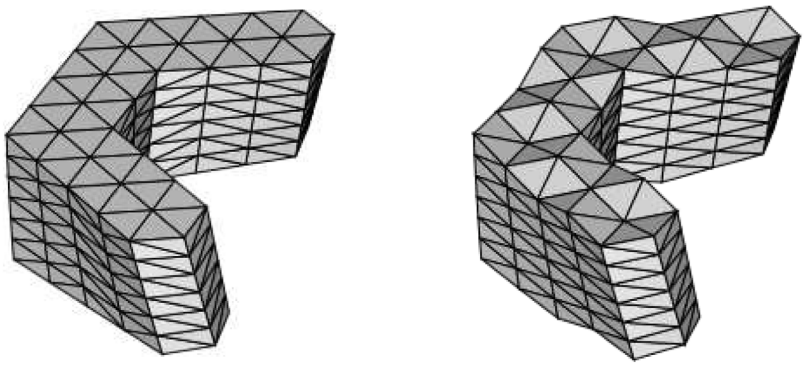

(a) Synchronous time-stepping, constant time instants.

(b) Asynchronous time-stepping, varying time instants.

Fig. 5. Synchronous versus asynchronous time-stepping in a mesh with $h_s = 1/4$, constructed of 238 nodes, 1179 edges, and 756 faces.

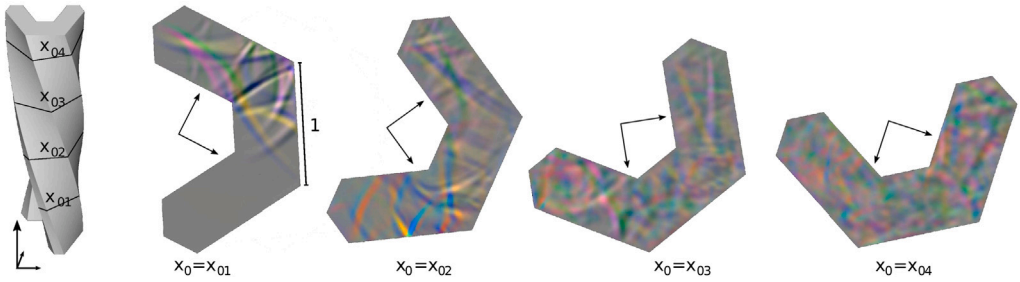

Fig. 6. Snapshots of the wave scattering by the moving cavity boundaries.

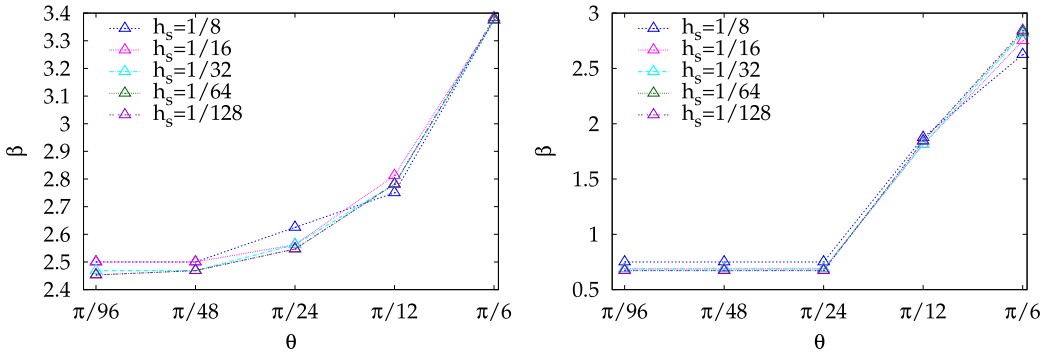

(a) Synchronous time-stepping.

(b) Asynchronous time-stepping.

Fig. 7. Stability factor β with respect to rotation speed angle θ for several spatial mesh refinements with the largest stable timestep.

$i = 1, 2, 3, 4$. The CPU time required for the entire simulation, including mesh generation, assembling discrete structures, spacetime evolution, and visualization, is 145 s.

We repeat the simulation for both synchronous and asynchronous time-steppings with rotation speed angles $\beta = \pi/(3 \cdot 2^i), i = 1, \ldots, 5$ and spatial edge lengths $h_s = 2^{-i}, i = 3, \ldots, 7$. With these tests, we consider the stability limits of the form $h_t \leq h_s/\beta$. Since the exact solution is not known, we consider the time-stepping to be stable, with the largest timestep with the norm of the solution vector bounded. As $\theta \to 0$ and $h_s \to 0$, the stability factor β converges in synchronous time-stepping to $\sqrt{6} \approx 2.449$ (the same stability factor as observed for the triangle mesh in Section 4.1) and in asynchronous time-stepping to 0.672 (see Fig. 7). Constructing asynchronous time-stepping requires more computing time but enables the use of larger timestep lengths compared to synchronous time-stepping. Overall, we do not observe a significant difference in CPU time requirements when comparing entire simulations using synchronous and asynchronous time schemes with the largest stable timestep (see Fig. 8).

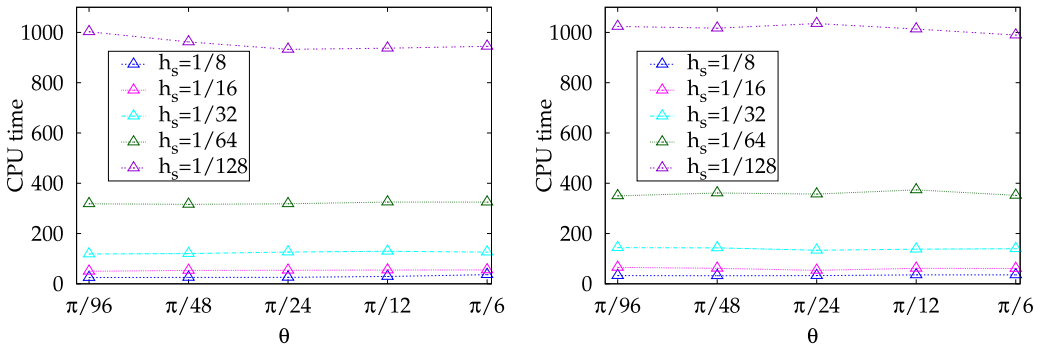

(a) Synchronous time-stepping. (b) Asynchronous time-stepping.

Fig. 8. CPU time in seconds required for the entire simulation, including mesh generation, assembling discrete structures, spacetime evolution, and visualization, with respect to rotation speed angle θ for several spatial mesh refinements with the largest stable timestep.

5. Conclusions

We presented a $(2 + 1)$-dimensional general wave model in Minkowski spacetime and employed DEC-based spacetime discretization on five different types of meshes. Numerical tests were conducted to assess stability conditions and consider accuracy. The method is not limited to convex spatial domains and allows for the treatment of moving and deforming domains through its construction. Nevertheless, the shape of the spatial domain and the mesh type should be adjusted to each other to ensure computational efficiency. Overall, the computational efficiency provided by the method is reflected in the fact that the numerical tests were conducted on a laptop computer in a short time.

Declaration of competing interest

The authors declare that they have no known competing financial interests or personal relationships that could have appeared to influence the work reported in this paper.

Acknowledgments

This project was partially funded by the Research Council of Finland (grants 259925 and 260076). The authors would like to thank their colleagues for their early-stage collaboration and the two anonymous reviewers for their comments, which improved the article.

Data availability

Data will be made available on request.

References

[1] Cartan H. Differential forms. In: Dover books on mathematics series, Dover Publications; 2006.
[2] Hestenes D, Sobczyk G. Clifford algebra to geometric calculus: a unified language for mathematics and physics, vol. 5, Springer Science & Business Media; 2012.
[3] Arnold DN, Falk RS, Winther R. Finite element exterior calculus: from Hodge theory to numerical stability. Bull Amer Math Soc 2010;47:281–354, URL http://www.ams.org/journals/bull/2010-47-02/S0273-0979-10-01278-4/.
[4] Perot JB, Zusi CJ. Differential forms for scientists and engineers. J Comput Phys 2014;257, Part B:1373–93. http://dx.doi.org/10.1016/j.jcp.2013.08.007, URL http://www.sciencedirect.com/science/article/pii/S0021999113005354.
[5] Stern A, Tong Y, Desbrun M, Marsden JE. Geometric computational electrodynamics with variational integrators and discrete differential forms. In: Geometry, mechanics, and dynamics. Springer; 2015, p. 437–75.
[6] Warnick KF, Russer PH. Differential forms and electromagnetic field theory. Prog Electromagn Res 2014;148:83–112.
[7] Dressel J, Bliokh KY, Nori F. Spacetime algebra as a powerful tool for electromagnetism. Phys Rep 2015;589:1–71.
[8] Schindler JC. Geometric calculus on pseudo-Riemannian manifolds. 2021, arXiv:1911.07145.
[9] Kettunen L, Rossi T. Systematic derivation of partial differential equations for second order boundary value problems. Int J Numer Modelling, Electron Netw Devices Fields 2023;36(3):e3078.
[10] Kettunen L, Mönkölä S, Parkkonen J, Rossi T. Systematic imposition of partial differential equations in boundary value problems. In: Impact of scientific computing on science and society. Springer; 2023, p. 25–44.
[11] Cartan É. Les systèmes différentiels extérieurs et leurs applications géométriques. Paris: Hermann & Cie éditeurs; 1945.
[12] Desbrun M, Hirani AN, Leok M, Marsden JE. Discrete exterior calculus. 2005, arXiv preprint math/0508341.
[13] Desbrun M, Kanso E, Tong Y. Discrete differential forms for computational modeling. In: Discrete differential geometry. Springer; 2008, p. 287–324.

[14] Tonti E. On the formal structure of physical theories. Consiglio Nazionale delle Ricerche; 1975.
[15] Tonti E. The mathematical structure of classical and relativistic physics, vol. 10, Springer; 2013.
[16] Yee KS. Numerical solution of boundary value problems involving Maxwell's equations in isotropic media. IEEE Trans Antennas and Propagation 1966;14(3):302–7.
[17] Bossavit A, Kettunen L. Yee-like schemes on a tetrahedral mesh, with diagonal lumping. Int J Numer Modelling, Electron Netw Devices Fields 1999;12(1–2):129–42.
[18] Hirani AN. Discrete exterior calculus. California Institute of Technology; 2003.
[19] Bell N, Hirani AN. PyDEC: software and algorithms for discretization of exterior calculus. ACM Trans Math Softw 2012;39(1):1–41.
[20] Räbinä J. On a numerical solution of the Maxwell equations by discrete exterior calculus [Ph.D. thesis], Jyväskylä studies in computing, (200). University of Jyväskylä; 2014, URL http://urn.fi/URN:ISBN:978-951-39-5951-7.
[21] Räbinä J, Kettunen L, Mönkölä S, Rossi T. Generalized wave propagation problems and discrete exterior calculus. ESAIM Math Model Numer Anal 2018;52(3):1195–218. http://dx.doi.org/10.1051/m2an/2018017.
[22] Myyrä M. Dexterior. 2024, https://github.com/m0lentum/dexterior.
[23] Boom PD, Kosmas O, Margetts L, Jivkov AP. A geometric formulation of linear elasticity based on discrete exterior calculus. Int J Solids Struct 2022;236:111345.
[24] Chen SC, Chew WC. Numerical electromagnetic frequency domain analysis with discrete exterior calculus. J Comput Phys 2017;350:668–89. http://dx.doi.org/10.1016/j.jcp.2017.08.068.
[25] Chen SC, Chew WC. Electromagnetic theory with discrete exterior calculus. Prog Electromagn Res 2017;159:59–78.
[26] da Silva L, Batista C, González I, Macêdo A, de Oliveira W, Melo S. A discrete exterior calculus approach to quantum transport and quantum chaos on surface. J Comput Theor Nanosci 2019;16(9):3670–82.
[27] Hirani AN, Nakshatrala KB, Chaudhry JH. Numerical method for Darcy flow derived using discrete exterior calculus. Int J Comput Methods Eng Sci Mech 2015;16(3):151–69.
[28] Desbrun M, Hirani AN, Marsden JE. Discrete exterior calculus for variational problems in computer vision and graphics. In: 42nd IEEE international conference on decision and control (IEEE cat. no. 03CH37475), vol. 5, IEEE; 2003, p. 4902–7.
[29] De Goes F, Desbrun M, Meyer M, DeRose T. Subdivision exterior calculus for geometry processing. ACM Trans Graph 2016;35(4):1–11.
[30] Saksa T. Comparison of finite element and discrete exterior calculus in computation of time-harmonic wave propagation with controllability. J Comput Appl Math 2025;457:116154.
[31] Räbinä J, Mönkölä S, Rossi T. Efficient time integration of Maxwell's equations with generalized finite differences. SIAM J Sci Comput 2015;37(6):B834–54.
[32] Lindqvist H, Martikainen J, Räbinä J, Penttilä A, Muinonen K. Ray optics for absorbing particles with application to ice crystals at near-infrared wavelengths. J Quant Spectrosc Radiat Transfer 2018;217:329–37.
[33] Mönkölä S, Räty J. Discrete exterior calculus for photonic crystal waveguides. Internat J Numer Methods Engrg 2023;124(5):1035–54.
[34] Mönkölä S, Räbinä J, Rossi T. Time-harmonic electromagnetics with exact controllability and discrete exterior calculus. C R Méc 2023;351(S1):647–65.
[35] Räbinä J, Kuopanportti P, Kivioja MI, Möttönen M, Rossi T. Three-dimensional splitting dynamics of giant vortices in Bose–Einstein condensates. Phys Rev A 2018;98:023624. http://dx.doi.org/10.1103/PhysRevA.98.023624, URL https://link.aps.org/doi/10.1103/PhysRevA.98.023624.
[36] Kivioja M, Mönkölä S, Rossi T. GPU-accelerated time integration of Gross–Pitaevskii equation with discrete exterior calculus. Comput Phys Comm 2022;278:108427.
[37] Kivioja M, Zamora-Zamora R, Blinova A, Mönkölä S, Rossi T, Möttönen M. Evolution and decay of an Alice ring in a spinor Bose–Einstein condensate. Phys Rev Res 2023;5(2):023104.
[38] Nitschke I, Reuther S, Voigt A. Discrete exterior calculus (DEC) for the surface Navier–Stokes equation. In: Transport processes at fluidic interfaces. Springer; 2017, p. 177–97.
[39] Bossavit A. Generalized finite differences in computational electromagnetics. Prog Electromagn Res 2001;32:45–64.
[40] Schulz E, Tsogtgerel G. Convergence of discrete exterior calculus approximations for Poisson problems. Discrete Comput Geom 2020;63:346–76.
[41] Hiptmair R. Discrete Hodge operators. Numer Math 2001;90:265–89.
[42] Toshniwal D, Hughes TJ. Isogeometric discrete differential forms: Non-uniform degrees, Bézier extraction, polar splines and flows on surfaces. Comput Methods Appl Mech Engrg 2021;376:113576.
[43] Lohi J, Kettunen L. Whitney forms and their extensions. J Comput Appl Math 2021;393:113520.
[44] Kettunen L, Lohi J, Räbinä J, Mönkölä S, Rossi T. Generalized finite difference schemes with higher order whitney forms. ESAIM Math Model Numer Anal 2021;55(4):1439–60.
[45] Lohi J. Systematic implementation of higher order Whitney forms in methods based on discrete exterior calculus. Numer Algorithms 2022;91(3):1261–85.
[46] Lohi J. New degrees of freedom for differential forms on cubical meshes. Adv Comput Math 2023;49(3):42.
[47] Regge T. General relativity without coordinates. Il Nuovo Cimento (1955-1965) 1961;19:558–71.
[48] McDonald JR, Miller WA. A discrete representation of Einstein's geometric theory of gravitation: the fundamental role of dual tessellations in Regge calculus. 2008, arXiv preprint arXiv:0804.0279.
[49] Sorkin RD. Spacetime and causal sets. In: Relativity and gravitation: Classical and quantum. World Scientific Singapore; 1991, p. 150–73.
[50] Rossi T, Räbinä J, Mönkölä S, Kiiskinen S, Lohi J, Kettunen L. Systematisation of systems solving physics boundary value problems. In: Numerical mathematics and advanced applications ENUMATH 2019. Springer; 2021, p. 35–51.
[51] Räty J, Mönkölä S. Local time-stepping for discrete exterior calculus on space-time mesh with refinements. J Comput Phys 2024. [under revision].
[52] Lou Y, Lehrenfeld C. Isoparametric unfitted BDF–Finite element method for PDEs on evolving domains. SIAM J Numer Anal 2022;60(4):2069–98.
[53] Badia S, Dilip H, Verdugo F. Space-time aggregated finite element methods for time-dependent problems on moving domains. 2022, arXiv preprint arXiv:2206.03626.
[54] Brackx F, Delanghe R, Sommen F. Differential forms and/or multi-vector functions. Cubo, Math J 2005;7(2):139–69.
[55] Kettunen L, Lohi J, Räbinä J, Mönkölä S, Rossi T. Generalized finite difference schemes with higher order Whitney forms. ESAIM Math Model Numer Anal 2021;55(4).
[56] Matsuo T, Mifune T. CFL conditions for finite integration methods on triangular meshes. IEEE Trans Magn 2009;45(3):1348–51.
[57] Erickson J, Guoy D, Sullivan JM, Üngör A. Building spacetime meshes over arbitrary spatial domains. Eng Comput 2005;20:342–53.
[58] Gopalakrishnan J, Schöberl J, Wintersteiger C. Mapped tent pitching schemes for hyperbolic systems. SIAM J Sci Comput 2017;39(6):B1043–63.